Bridging Hemodynamics, Tissue Mechanics, and Pathophysiology in Coronary Artery Disease: A New Agent-Based Model with Tetrahedral Mesh Integration

Jeremy Warren[1], Anna Corti[2], Clark A. Meyer[1], Heather N. Hayenga[1*]

[1]Department of Bioengineering, University of Texas at Dallas, Richardson TX 75080, USA

[2]Department of Electronics, Information and Bioengineering, Politecnico di Milano, Milan, Italy

Abstract

We introduce a new multi-physics, multi-scale modeling approach to understand plaque progression during coronary artery disease. Prior works have coupled agent-based models (ABMs) with finite element analysis (FEA) or computational fluid dynamics (CFD) to study the individual contributions of tissue mechanics or hemodynamics to plaque growth. However, these approaches could not simultaneously capture the dynamic interplay between all three domains that drive plaque development. This study aims to present a novel method that merges hemodynamics via CFD, biological processes via ABM, and biomechanics via FEA into a single multi-scale, multi-physics simulation (CAFe). A description of the mechanisms and modeling approaches utilized in the CAFe model is provided, as well as preliminary exploration of the model's capabilities in idealized healthy and stenosed coronary artery models. A volumetric 3D tetrahedral mesh of the artery is shared between CFD, ABM, and FEA to simulate geometrical and biological changes with continuity and consistency. The CFD and FEA modules, implemented with FEBio, calculate the wall shear stress and structural stress and strain, respectively. These biomechanical values are passed to the ABM, implemented in MATLAB, which simulates vascular remodeling using molecular diffusion, cell migration, equations for cellular processes, and volumetric

growth to update the geometry. Initial results using CAFe suggest atherosclerotic arteries seek to maintain a hemodynamic threshold through preferential growth and remodeling downstream of a stenosis. The innovative approach described herein marks a significant step forward in predictive modeling of CAD progression and paves the way for powerful coupling of the spatiotemporal-dependent remodeling paradigms exhibited by the disease.

Keywords: Coronary Artery Disease (CAD), Computational Modeling, Cardiovascular, Finite Element Analysis (FEA), Agent Based Modeling (ABM), Biomechanics, FEBio

*Address correspondence to:

Dr. Heather N. Hayenga

The University of Texas at Dallas

800 W. Campbell Road, Richardson, TX 75080

Phone: 972-883-3558

E-mail: heather.hayenga@utdallas.edu

1. Introduction

Coronary artery disease (CAD) is a major cardiovascular disease (CVD); it was responsible for 382,820 deaths in 2020 in the USA, accounting for approximately 55% of all CVD-related deaths that year (Tsao et al. 2022). CAD is characterized by a buildup of fatty plaque and dead cells inside coronary arteries. Also called atherosclerosis, CAD obstructs the flow of oxygenated blood, often leading to major adverse cardiovascular events (e.g., myocardial infarction). An estimated 7.2% of adults in the United States over the age of 20 have some form of CAD, rising to over 35% for adults over the age of 30 (Blewett et al. 2021). Given the prevalence and severity of CAD, understanding the biomechanical and structural factors driving plaque progression and instability is essential for advancing diagnostic and therapeutic approaches.

Coronary arteries are constantly responding to changes in biochemical, mechanical, and hemodynamical loads to maintain homeostatic equilibrium. In CAD, dysfunction in this highly interconnected system is responsible for plaque deposition and adaptive arterial remodeling. An improved understanding of the underlying pathological mechanisms of CAD will enable a more accurate prediction of plaque growth and subsequent management of the prevalent disease.

Multiscale agent-based modeling (ABM) has offered valuable insights into the complex interplay of events that drive the progression of CAD. Previously, computational fluid dynamics (CFD) models have been coupled with ABMs to understand mechanisms such as hemodynamically driven leukocyte transendothelial migration (Bhui and Hayenga 2017), the impact of pulsatile flow on leukocyte capture (Ciri et al. 2018), and plaque growth (Corti et al. 2019; 2020). Separately, a finite element analysis (FEA) model has been coupled with ABM to investigate the biomechanical mechanisms contributing to arterial growth and remodeling (Keshavarzian, Meyer, and Hayenga 2018). Both implementations (CFD with ABM and FEA with ABM) provided a path for more advanced models capable of studying CAD outcomes such as vascular adaptation (Corti et al. 2021) or restenosis (Corti et al. 2022). However, a fully coupled model

that incorporates CFD, ABM, and FEA would allow for a deeper understanding of artery remodeling, as was recently demonstrated with femoral artery restenosis (Corti et al. 2024).

Herein we present CAFe (CFD, ABM, and FEA), a multi-scale, multi-physics, modeling framework of atherosclerotic plaque growth that is capable of seamlessly coupling all three domains: (i) a CFD module for hemodynamics, (ii) an ABM module for biological processes, and (iii) a FEA module for structural mechanics [Figure 1].

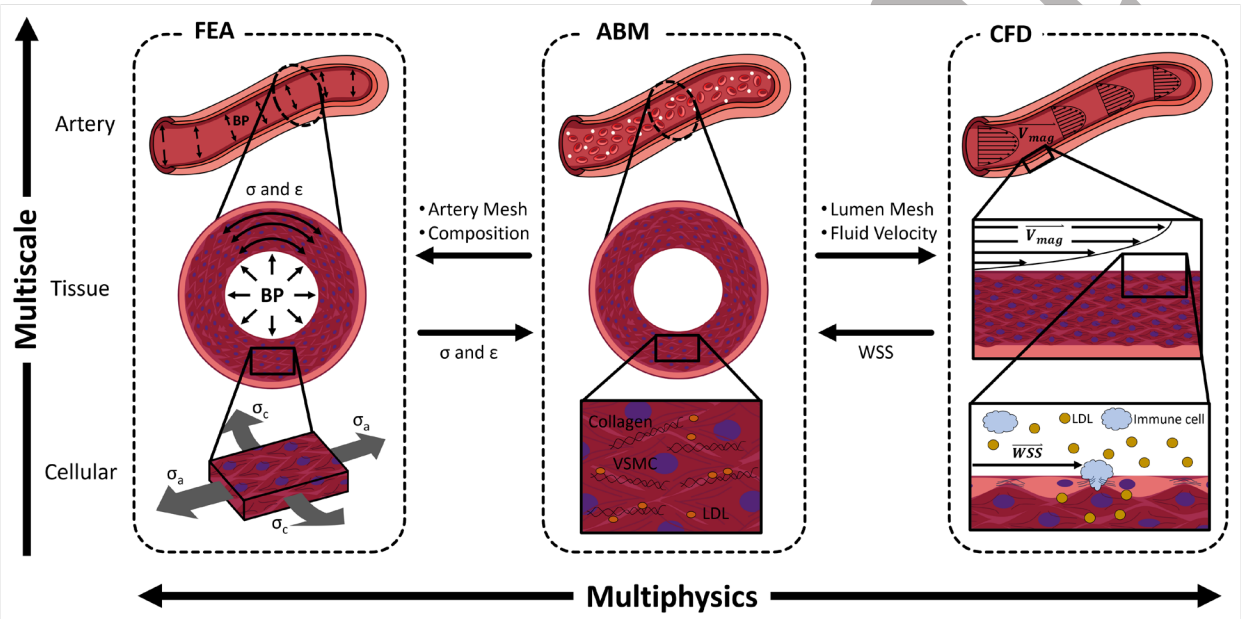

Figure 1. Overview of the interconnected submodules of the multi-scale, multi-physics CAFe model. Stresses and strains calculated in the FEA module and wall shear stress (WSS) values from the CFD module drive the biological interactions of the ABM.

This framework introduces a substantial novelty in the coupling mechanism of the three modules by utilizing a volumetric 3D mesh capable of capturing the geometrical changes produced by plaque growth. As proof of concept, the CAFe model described herein was applied to two cases of idealized (with respect to 3D shape and composition) human coronary arteries (Section 2.2). The first case, a non-atherosclerotic human coronary artery is modeled as a straight axisymmetric cylindrical tube with healthy physiological inputs to explore the model's response to healthy, homeostatic conditions. In the second case, an

atherosclerotic human coronary artery is modeled as a non-axisymmetric tube with a mild 30% stenotic plaque (Cury et al. 2016). Both cases simulated a timeframe of 6 months, a clinically relevant endpoint based on the Atorvastatin and PREMIER trials (Svetkey et al. 2003; Eshtehardi et al. 2012), to observe intra-plaque remodeling while enabling rapid model development.

2. Methods

2.1 A multi-scale, multi-physics framework

CAFe is a multi-scale, multi-physics framework that enables exploration into the underlying mechanisms contributing to plaque growth by coupling three separate, yet interconnected modules: (i) The ABM module (Section 2.3) simulates biological processes driving tissue remodeling at the cellular/tissue scale, (ii) the FEA module (Section 2.4) calculates mechanical stresses and strains from updated composition and shape, and (iii) the CFD module (Section 2.5) calculates hemodynamical wall shear stress (WSS) reflective of changes in the luminal geometry.

The initial geometry, mesh (nodes and elements), and configuration of each patch (e.g., number of cells, extracellular matrix (ECM) composition, and molecular concentration), are directly given as inputs or calculated from ABM rules. Initially, the average edge length of the patches (i.e. elements) is approximately 0.25mm, yet the size of a patch changes during active remodeling. The initial states of stress, strain, and WSS are calculated by independently executing FEA and CFD simulations using the open-source FEBio software (Maas et al. 2012).

At the end of each ABM time step, the change in volume of each patch is calculated. This change in volume is used to update the mesh via the volumetric growth submodule (Section 2.3.4). Every 15 ABM timesteps, the FEA and CFD modules are executed separately to update the mechanical and hemodynamical values,

respectively, which are then passed back to the ABM for the next CAFe time step. At the end of each CAFe time step, the composition of each patch is updated [Figure 2].

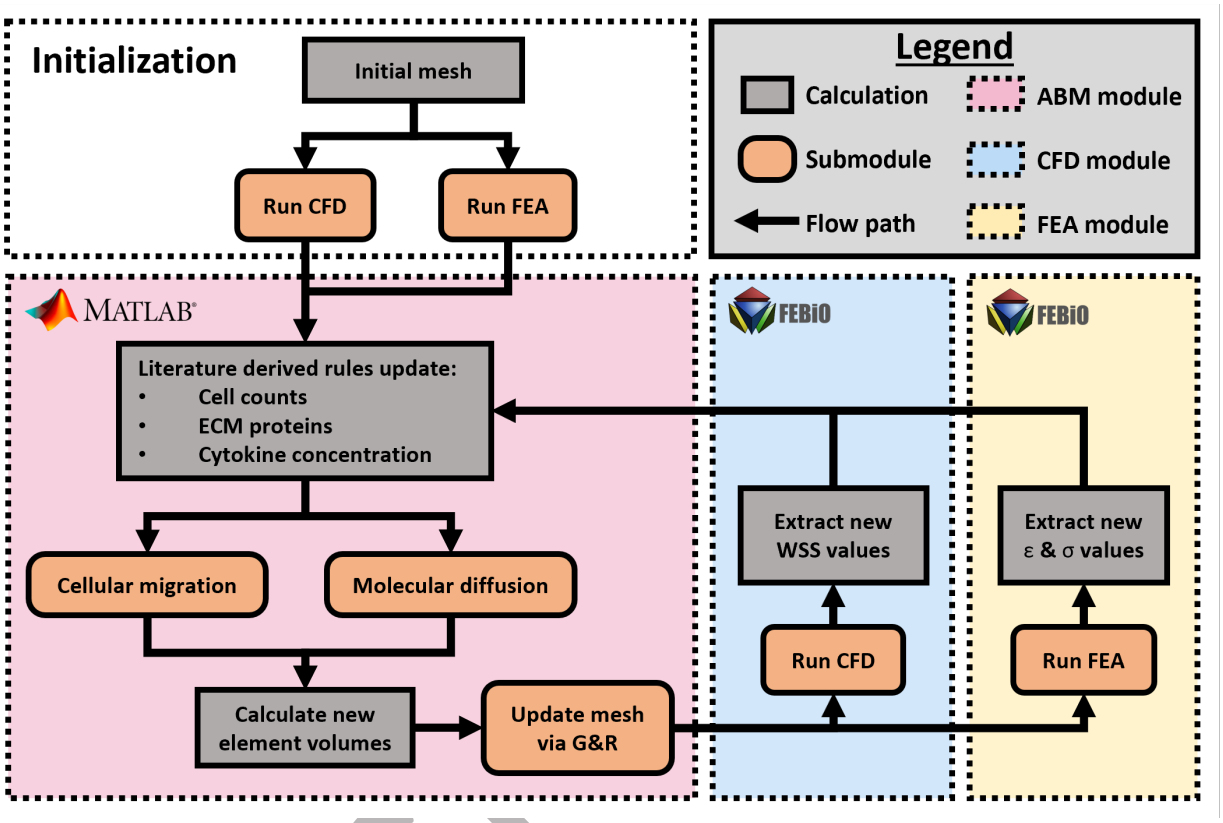

Figure 2. General flowchart of the CAFe model. After initialization, the ABM updates the geometry via cellular migration, molecular diffusion, growth and remodeling submodules. Modular CFD and FEA simulations update hemodynamical and mechanical values, respectively.

2.2 Coronary artery meshes and compositions

As a proof-of-concept, two idealized human coronary artery geometries are presented. The first case represents a segment of a healthy human coronary artery, whereas the second case represents a stenotic coronary artery with a 30% stenosis [Figure 3]. Both meshes were comprised of tetrahedral elements with an average edge length of 0.25 mm. Case 1 had 75,667 elements and 15,334 nodes, and Case 2 had 76,095 elements and 15,391 nodes. The number of elements and nodes did not change during the simulation. In

both cases, the region of the artery being simulated had an axial length of 8 mm, maximum lumen diameter of 3 mm, and radial intimal/medial and adventitial layer thickness of 0.5 mm each (Gradus-Pizlo and Feigenbaum 2003; Konishi et al. 2023). The plaque in the stenotic mesh was 3 mm in axial length, 1.5 mm at the thickest radial point, and 1.5 mm wide circumferentially. In both cases, the region of the artery being simulated was encapsulated by a sleeve portion that acts as a surrogate for the connective and perivascular tissues in a real coronary artery and the sleeve isolates the region of interest from boundary conditions during the volumetric growth and mechanical analyses. A similar approach was utilized in in-silico mechanical simulations of patient-specific arteries (Warren et al. 2022; Guvenir Torun et al. 2021). This sleeve layer had a radial thickness of 0.25 mm and an additional axial length of 0.5 mm anterior and posterior to the region of interest.

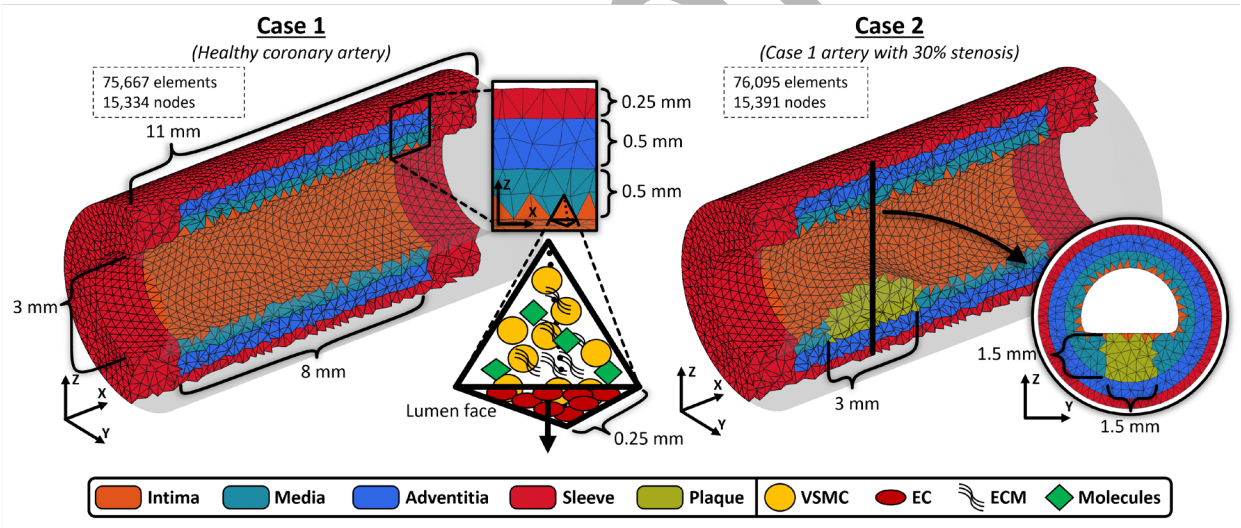

Figure 3. Idealized meshes of healthy (Case 1) and atherosclerotic (Case 2) human coronary arteries. The intimal/medial layer, adventitia, and sleeve layers are approximately 0.5, 0.5, and 0.25 mm thick, respectively. Each tetrahedral element (i.e. patch) has an initial edge length of approximately 0.25mm and contains cell agents, ECM and molecular components. Patches that line the lumen with an entire face are considered intimal patches and contain ECs determined by the surface area of the lumen face.

The initial quantities of cell agents and ECM constituents within each patch are given as inputs to the CAFe model [Table 1]. The initial number of cells in a patch was calculated by multiplying the percent

composition of the corresponding tissue type by the volume of the patch and dividing by the cell's volume [Table 2]. The initial composition of ECM in each patch was determined similarly, using the mass of ECM constituents. Molecular concentrations within a patch are calculated when CAFe initializes using the ABM rules. Patches in the intimal and medial layers have vascular smooth muscle cells (VSMCs) and ECM components. Those patches facing the luminal surface also contain endothelial cells (ECs), proportional to the area of the lumen-adjacent face [Figure 3]. Patches in the adventitial layer contain fibroblasts (FBs) and ECM. The plaque patches contain VSMCs and leukocytes. The sleeve layer is empty of cells and does not remodel within the ABM, but, as a connective tissue surrogate, contributes mechanically during FEA simulations. Other parameters considered in the model are blood LDL content (9.5e5 pg/mm^3 for healthy, 1.2e6 pg/mm^3 for stenosed (Expert Panel on Detection 2001)) and blood leukocyte density (11e3 cells/mm^3 (Blumenreich 1990), 50% neutrophils, 30% lymphocytes, and 10% monocytes).

		Plaque (Liu et al. 2011; Villiger et al. 2018)	**Artery Wall** (Keshavarzian et al. 2018; Wagenseil and Mecham 2009)		
			Intima	**Media**	**Adventitia**
Artery Wall Cells	**EC**	-	Area dependent	-	-
	VSMC	35%	50%*	25%	-
	FB	-	-	-	25%
Leukocytes	**Foam cell**	15%	-	-	-
	Lymphocyte	2.5%	-	-	-
	Neutrophil	5%	-	-	-
	Monocyte	2.5%	-	-	-
	Macrophage	10%	-	-	-
ECM	**Collagen**	10%	30%*	35%	35%

	Elastin	10%	10%*	35%	35%
	Gelatin	10%	10%*	5%	5%

*Table 1. Initial percent volume composition of each element type. *Actual percentage determined based on the remaining volume available after accounting for the number of ECs in the lumen face for each patch.*

2.3 The ABM module

The ABM module is responsible for simulating processes such as cell turnover, cell migration, production or reduction of molecules and ECM proteins, molecular diffusion, and volumetric growth [Supplemental Figure 1]. A 6-hour timestep was used. Within the ABM, four submodules are coupled to simulate plaque remodeling: (i) biological rules, (ii) cellular migration, (iii) molecular diffusion, and (iv) volumetric growth.

2.3.1 The biological rule sub-module, agents, and components

Biological processes are modeled using equation-based rules derived from literature (Bhui and Hayenga 2017; Keshavarzian et al. 2018; Thorne et al. 2011). These processes include cellular proliferation, production or removal of solutes, ECM remodeling, leukocyte infiltration, and LDL infiltration.

Although other types of equations can be utilized, this study uses four types of equations to represent these processes: (i) polynomial, (ii) sigmoidal, (iii) piecewise continuous, or (iv) probabilistic. First-order polynomials are used for basal production rates such as the baseline production of matrix metalloproteinase (MMP) by VSMCs and FBs [Supplemental Table 1, rules 5, 13-15]. Higher-order polynomials are used for more complicated processes such as monocyte adhesion as a function of WSS or LDL concentration at the wall [Supplemental Table 1, rules 32, 53]. Sigmoidal equations are used to implement threshold effects and saturation points, making them suitable for modeling processes such as leukocyte adhesion as a function of interleukin-1 (IL1) concentration [Supplemental Table 1, rules 31, 38, 44]. Piece-wise continuous rules are used when appropriate to define outputs with varying responsive

ranges. For example, neutrophils only adhere to the endothelium when the WSS is lower than 1.2 Pa but lack the bond strength to maintain contact with the endothelium when WSS is greater than 1.2 Pa [Supplemental Table 1, rule 46]. For probabilistic rules, a random number generator is used to model stochastic processes such as cell proliferation [Supplemental Table 1, rules 1, 2, 10, 11]. When an equation requires a mechanical or hemodynamic input, the value of the corresponding patch is used. For example, VSMC production of MMP2 as a function of mechanical stress [Supplemental Table 1, rule 6] uses the effective stress corresponding to the patch the VSMC resides to calculate P_{MMP2}^{VSMC}. Temporally, the hourly output of each rule is scaled to match the 6-hour ABM time step by multiplying by 6. The full list of equations governing the biological processes in the ABM module can be found in Supplemental Table 1 and were adapted from the work of Bhui et. al. (Bhui and Hayenga 2017) and Keshavarzian et. al. (Keshavarzian et al. 2018).

Each cell agent has 4 parameters: migration velocity, mass, volume, and lifespan [Table 2]. To reduce computation, the location of an agent is not modeled explicitly within a patch. Instead, the location of an agent is assumed to be at the "center" of a patch. Regarding cell actions via biological rules, all types of cells, except for macrophages, are modeled as a collection within a patch; the output of equations with these cell types is calculated using the total number of cells of a type within a patch as input. For example, the total amount of MMP1 produced by VSMCs in a patch [Supplemental Table 1, rule 5] is calculated by multiplying the output of the equation for a single VSMC, P_{MMP1}^{VSMC}, by the total number of VSMCs in the patch. Conversely, macrophages are modeled and tracked individually, i.e., equations involving macrophages are calculated as the output of each individual agent, and then summed together to get a total value for a given patch. This approach accounts for the phenotypical transformation of macrophages into foam cells once they consume a certain amount of oxLDL [Supplemental Table 1, rule 57, 58]. Apart from VSMCs and FBs whose lifespan is rule-based, and ECs and foams cells who live indefinitely, cell turnover as determined by a cell's lifespan is used to update the total number of cells at each ABM step.

	Cell Agent	Migration Velocity [mm/h]	Mass [g]	Volume [mm^3]	Lifespan [h]
Artery Wall Cells	**VSMC**	Non-migratory	1.31e-6	1.31e-6	Rule-based
	EC	Non-migratory	5.25e-11	1.25e-7	Inf.
	FB	Non-migratory	9e-10	9e-7	Rule-based
Immune Cells	**Lymphocyte**	0.1	9e-10	9e-7	336
	Neutrophil	0.6 (Moghe, Nelson, and Tranquillo 1995)	9e-10	9e-7	144
	Monocyte	0.1 (Farrell, Daniele, and Lauffenburger 1990)	9e-10	8.18e-6	336
	Macrophage	0.1 (Farrell et al. 1990)	9e-10	8.18e-6	336
	Foam Cell	Non-migratory	9e-10	8.18e-6	Inf.

Table 2. Parameters defined for each cell agent in the ABM.

Molecular components have three parameters, a diffusion coefficient, molar mass, and half-life [Table 3]. Molecular components are represented by the sum of their masses in each patch. The biological rules are used to calculate the amount of each molecular component that is produced in a single ABM time step. Concurrently, the amount of a molecular component that is degraded in a single ABM time step is calculated using its half-life. The remaining amount in each patch is then passed to the diffusion sub-module (Section 2.3.3) to update the concentration gradient for the next timestep.

Name	Diffusion Coefficient [mm^2/h]	Molar Mass [kDa]	Half-Life [h]	Ref
PDGFab	0.108	26.8	2.4	(Gay and Winkles 1991)
IL1	0.108	17.5	2.5	(Hazuda, Lee, and Young 1988)
IL10	0.108	17.5	2.5	(Hazuda et al. 1988)
TNFa	0.108	17.5	2.5	(Hazuda et al. 1988)
TGFβ	0.108	25	2.5	(Hazuda et al. 1988)
LDL	4.4e-2	2930	68	(Mallol et al. 2012)
oxLDL	4.4e-2	2930	68	(Mallol et al. 2012)

Table 3. Parameters defined for each molecule in the ABM.

Like molecular components, ECM components are represented as the sum of their mass in each patch. The production of structural ECM components (i.e., collagen, elastin, and gelatin) is driven by the actions of cellular agents [Supplemental Table 1, rules 5-8], whereas their reduction is driven by degradation via matrix metalloproteinases [Supplemental Table 1, rules 22-29].

2.3.2 The cellular migration sub-module

Chemotactic migratory patterns of immune cells are modeled in the cell migration submodule. This submodule replicates experimental evidence of leukocytes migrating individually toward a source of a chemoattractant (Cano, Vargas, and Lavoie 2016; Lu, Um, and Tartakovsky 2021) with a “random walk” pattern by incorporating a simplified algorithm adapted from (Rangarajan and Zaman 2008; Zaman et al.

2005) [Supplemental Figure 2] that simulates cellular migration over the course of an ABM time step. The time step discretization is calculated using patch connectivity, distances between patch centroids, and the migration velocity of a given cell agent. The decisions of each individual cell agent are modeled. Cells have a higher probability of migrating into an adjacent patch with a higher chemoattractant concentration than to a patch with a lower chemoattractant concentration. However, if multiple adjacent patches have a higher chemoattractant concentration than the patch they resided in, a patch is randomly chosen for the cell to migrate into. Artery wall cells (VSMCs, ECs, and FBs) are not modeled in the migration submodule, although they could be incorporated in future models.

2.3.3 The molecular diffusion sub-module

Molecular diffusion is modeled during each ABM time step. Concentration gradients are calculated using the molar mass of each molecule and patch volume. Diffusion is simulated using Fick's second law as a second order parabolic PDE in MATLAB's PDE solver. The concentration gradient is used as the initial starting concentration and the 6-hour ABM time step is discretized using patch connectivity. To ensure mass conservation, a zero-flow Neumann boundary condition (Rapp 2017) is enforced at the external boundary of the artery region of interest. Of note, ECM components are stationary and do not diffuse.

2.3.4 The volumetric growth sub-module

In each ABM time step, changes in ECM composition and the number of cells modify the volume of each patch. The number of nodes and patches or elements does not change during remodeling. The element-connectivity of the mesh remains the same, only the nodal coordinates are modified. To ensure the geometric volume of each patch matches the volume calculated by the ABM, the mesh is updated using a modified version of the "Cell-Growth" plugin in FEBio (Ateshian et al. 2012). After the biological rules, migration, and diffusion submodules are executed, a subroutine calculates the fold change in volume throughout the region of interest and writes a material definition for each patch to a FEBio input file. This

material definition ties the volume fold-change to the osmotic pressure component of the Cauchy stress equation by imposing positive or negative isotropic pressure to make an element grow or shrink. An incompressible hyperelastic Neo-Hookean material with a Young's modulus of 10 MPa is assigned to the sleeve elements surrounding the region of interest, serving as a mechanical backbone to constrain growth and mimic the properties of healthy arterial tissue. The nodes on both ends of the sleeve region are fixed and a pressure load is applied on the lumen to distribute the resulting forces.

2.4 The FEA module

Mechanical stresses and strains drive changes in cell and ECM patch composition which modifies the mechanical properties of the artery. To dynamically update changes in material properties of the mesh the elastic modulus of each patch is computed from the percent composition of cell agents and ECM constituents and their associated elastic modulus [Table 4]. This value is used as the Young's modulus of a hyper-elastic isotropic Neo-Hookean material model with a Poisson's ratio of 0.48. The nodes on both ends of the sleeve are fixed and a ramped systolic pressure load of 120 mmHg is applied to the luminal surface. Mechanical analysis is performed with FEBio's built-in implicit solver. Once complete, an automated script reads the Cauchy stress and Green-Lagrange strain values and calculates the effective stress [Supplemental Table 1, rule 59] and effective strain [Supplemental Table 1, rule 60] of each patch. These effective stress and strain values are then passed back to the ABM for the next timestep.

Agent Type		**Elastic Modulus [kPa]**	**Ref.**
ECM	Collagen	442.6	(Lu et al. 2004)
	Elastin	100	(Karšaj, Sorić, and Humphrey 2010; Lu et al. 2004)

	Gelatin	2	(Lou and Chirila 1999; Norris and McGraw 1964; Yakimets et al. 2005)
Cells	VSMC	4.3	(Qiu et al. 2010)
	FB	0.5	(Engler et al. 2004)
	EC	1.42	(Stroka and Aranda-Espinoza 2011)
	Neutrophil	1.5	(Lee, Patel, and Park 2011)
	Lymphocyte	0.085	(Bufi et al. 2015)
	Monocyte	0.52	(Bufi et al. 2015)
	Macrophage & Foam cell	1.2	(Bufi et al. 2015; Patel et al. 2012)

Table 4. Elastic modulus values for each agent used in the FEA module.

2.5 The CFD module

WSS plays a critical role in plaque remodeling (Timmins et al. 2017; Tziotziou et al. 2023) and LDL uptake (Deng et al. 1995) in CAD. Rigid CFD simulations using FEBio's fluid solver are utilized to calculate WSS values. To generate the mesh for the fluid cavity, the luminal surface is isolated and extended 5 diameters (roughly 15mm) at the inlet and outlet to allow fluid flow to fully develop. This extended lumen surface is used to generate a volumetric mesh comprised of tetrahedral elements (Si 2015) and pentahedral elements at the luminal boundary [Figure 4A]. Blood is modeled as a homogeneous, incompressible, and Newtonian fluid, with a viscosity of 3.5e-3 Pa·s and a density of 1060 kg/m^3. Parabolic, laminar pulsatile blood flow, with a cardiac period of 1 second for 3 cycles is applied to the inlet (He and Ku 1996; Nosovitsky et al. 1997). Since blood flow is naturally pulsatile, WSS changes significantly throughout the cardiac cycle. Bhui et al. and Ciri et al. found that the total number of leukocytes migrating into the artery wall over the course of an hour can be replicated using instantaneous WSS at 45% of the cardiac cycle (Ciri et al. 2018;

Bhui and Hayenga 2017). To further ensure consistent WSS calculations, three cardiac cycles are simulated and the average WSS at 45% of each cardiac cycle [Figure 4B] is used.

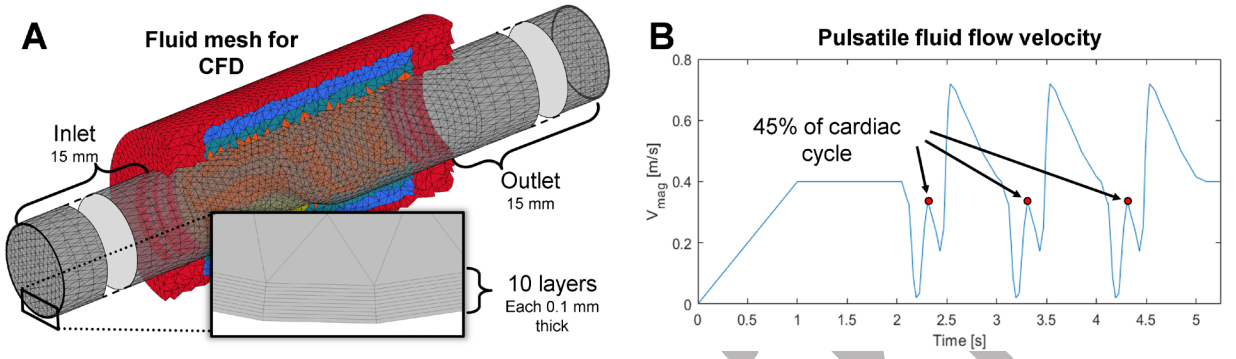

Figure 4. CFD simulation mesh and fluid velocity at the inlet. A) The luminal surface of the mesh is isolated and extended 15 mm at the inlet and outlet. 10 layers of pentahedral elements line the luminal boundary to accurately capture WSS. B) Pulsatile bulk velocity at the inlet with 45% of the cycle denoted with arrows.

3. Results

Simulations were conducted to evaluate CAFe's ability to simulate tissue remodeling, modify geometry, and to test the coupling between CFD, ABM, and FEA. A Windows x64-based PC with 128 GB RAM and 20 CPU cores was utilized. FEA, CFD, and growth models were performed using FEBio v2.3.0. The ABM and its submodules as well as the automated interfacing functions were executed in MATLAB vR2022b. Two cases were considered: 1) a healthy artery with no plaque, and 2) an artery with a 30% stenosis.

3.1 Comparison between the healthy and stenosed cases

Two simulations were run for each case and a two-tailed Student's T-test was performed showing little run-to-run variability [Figure 5]. The number of patches and nodes remains the same in all instances. On average, the total number of VSMCs decreased by 7.9% and 5.3% in the healthy and stenosed cases ($p=0.0034$), respectively [Figure 5A], whereas the total number of fibroblasts increased by 0.53% and 1.5% in the healthy and stenosed cases ($p=0.0011$), respectively [Figure 5B]. TGFβ more than doubled in the

stenosed case but remained at zero in the healthy case ($p=0.0498$) [Figure 5C]. Within the first 3 days, the total amount of PDGFab in the stenosed case dropped significantly but increased slightly in the healthy case with both instances converging to a homeostatic value around 5.5e6 pg by day 5 ($p<0.001$) [Figure 5D]. The total volume of the mesh in the region of interest remained the same and decreased by 3.6% in the healthy and stenotic case ($p=0.0639$), respectively [Figure 5E]. Although the decrease in volume for the stenotic case was minimal, the final volume of the plaque (patches containing foam cells) was greater than two times the original volume. Moreover, the plaque extended downstream from its original position [Figure 5F]. Mechanical stresses in the healthy artery were more uniformly distributed than the stenosed case [Supplemental Figure 3]. The effective stress in the healthy case ranged from 35-45 kPa whereas the stenosed case had stresses as low as 5 kPa in the plaque region and stresses as high as 55 kPa in the regions directly adjacent to the plaque and in the healthy tissue.

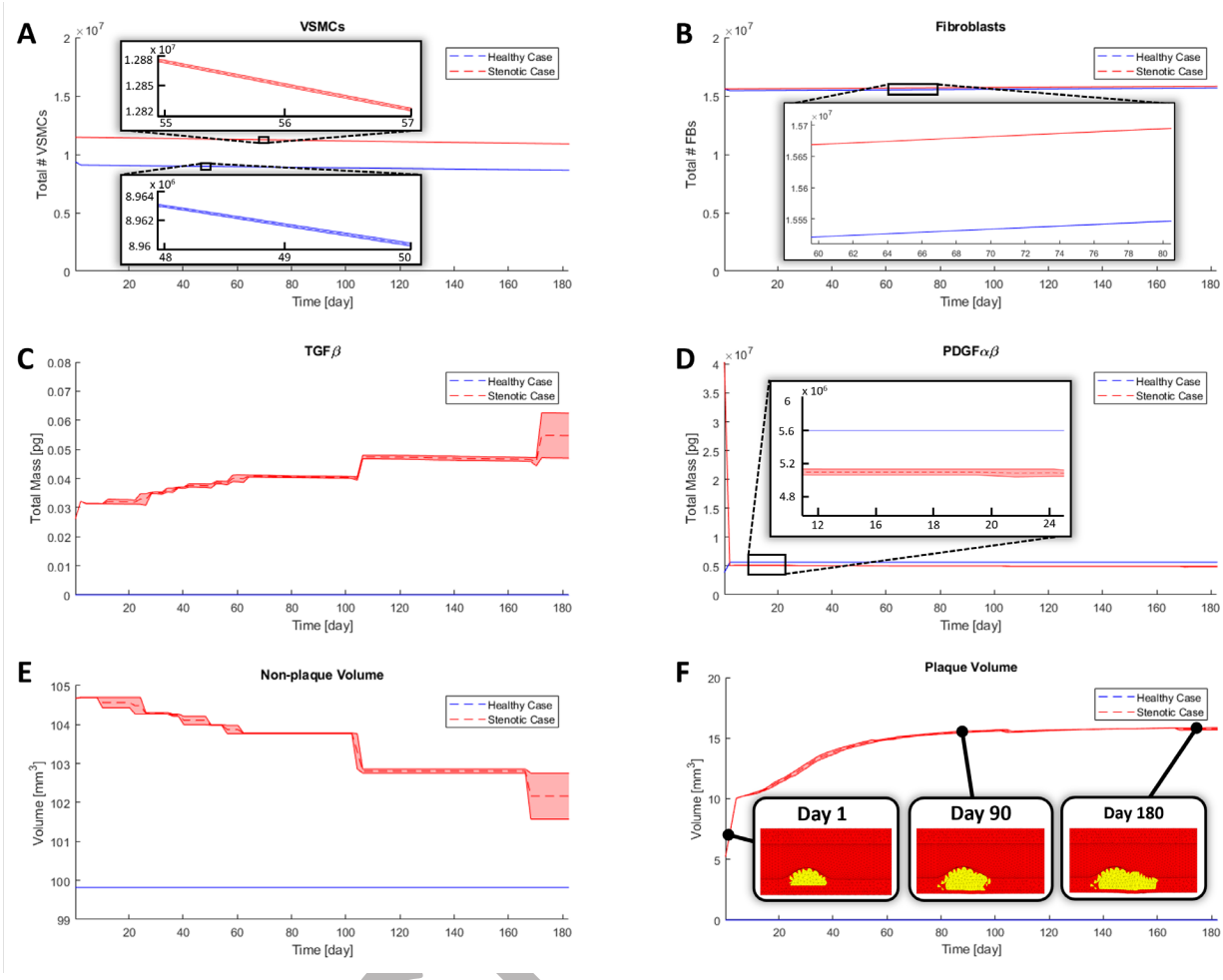

Figure 5. Comparison between healthy and stenosed cases for cellular, molecular, and volumetric changes. The mean (dashed line) ± max-min range (shadow) of two simulations are presented for the healthy and stenosed case. A) Total number of VSMCs. B) Total number of FBs. C) Total amount of TGFβ. D) Total amount of PDGFab. E) Total non-plaque volume in the region of interest. F) Total plaque volume in the region of interest with mesh overlay of the stenosed case at day 0, 90, and 180; plaque includes any patches with foam cells (plaque shown as yellow in mesh view, non-plaque is red).

3.2 Leukocyte infiltration in the stenosed case

Regions of low WSS (i.e. <1 Pa for monocytes, <0.41Pa for lymphocytes, and <1.2 Pa for neutrophils [Supplemental Table 1, rule 33, 40, 46]) paired with the presence of IL1 and TNFA drive leukocyte infiltration into the artery. Two simulations were run for the stenosed case [Figure 6]. The surface area of the lumen exposed to a WSS less than 1.2 Pa (the maximum WSS at which leukocytes attach to the wall)

shrinks as the model runs [Figure 6A]. The total amount of TNFα and IL1 reached a homeostatic value around day 15 [Figure 6B]. The total number of lymphocytes and neutrophils increase for the first 35 days and then reach a homeostatic value by day 50 [Figure 6C]. Although not clearly shown in the figure, monocytes also infiltrate the wall. However, the rate at which monocytes turn into macrophages was less than the rate of macrophage to foam cell transition, hence monocytes and macrophages decrease while foam cells consistently increase with time. Foam cells do not have a defined lifespan and accumulate as the model runs.

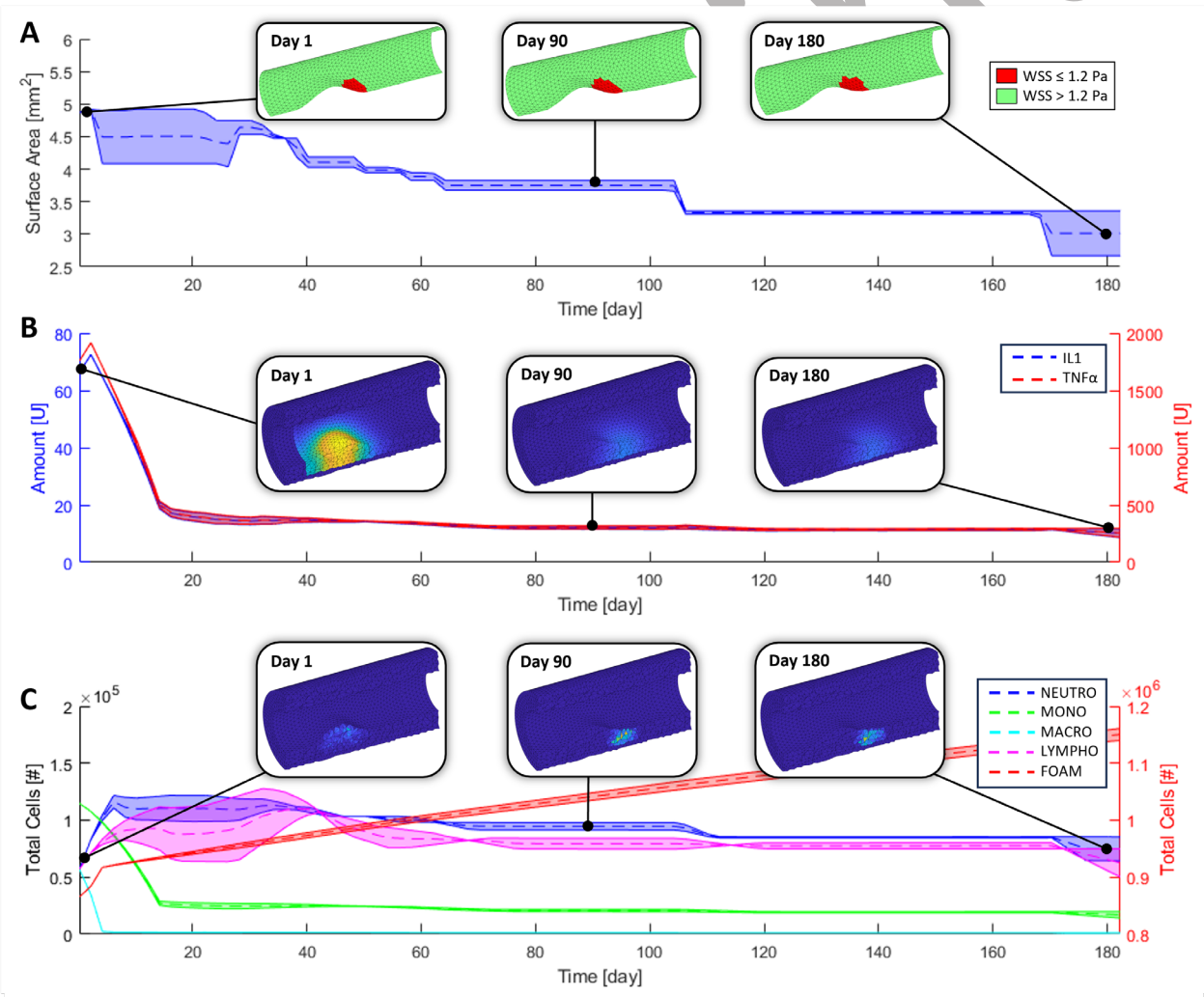

Figure 6. Axial cross-section views of the stenosed mesh at key time points paired with hemodynamically driven cytokine and leukocyte amounts. The mean (dashed line) ± max-min range (shadow) of two simulations are presented for the stenosed case. A)

The surface area of the lumen with a WSS that is less than the maximum threshold for leukocyte attachment (i.e., 1.2Pa). B) Evolution of representative TNFα and IL1 concentration in the artery with TNFα concentration shown in mesh view. C) Total number of leukocyte agents in the artery with neutrophils shown in the mesh views.

4. Discussion

In the context of coronary artery disease (CAD), we presented an integrated multi-scale, multi-physics framework that offers a transformative approach to understanding the intricate dynamics of plaque progression. By combining hemodynamics, biomechanics, and cellular biology into a unified framework, we can simulate the nuanced interactions between fluid, tissue, and biology and build insight into how plaque changes over time.

Our framework demonstrated an integrated approach to better understand the pathophysiological processes of CAD. For example, our simulations suggest that regions of the artery that exhibit low WSS are critical zones for plaque growth which is consistent with current literature that point to hemodynamic forces playing a pivotal role in disease progression (Samady et al. 2011). We also observed enhanced leukocyte captured downstream of the maximum luminal stenosis in the stenosed case where flow separation occurred if the WSS was less than 1.2 Pa. The increased number of leukocytes in this region corresponded with the location of the highest concentration of cytokines which, in turn, corresponded with increased leukocyte presence. Additionally, more LDL infiltrated in this region of the wall, contributing to increased differentiation of macrophages into foam cells. Indeed, these results corroborate longitudinal clinical studies that show preferential plaque growth in the downstream direction (Smedby 1997).

Mechanically, our simulations suggest a more homogenous distribution of mechanical stress in the healthy artery as compared to the plaque of the stenosed case. Consistent with clinical observations, the dysregulation of structural ECM and the presence of fatty lipids in the plaque correspond with the reduction in effective stress observed herein (Liu et al. 2011; Villiger et al. 2018). Hemodynamically, the

CAFe model produces similar flow profiles and WSS values to established CFD models. Ciri et al. utilized both custom and commercial CFD software to model an idealized artery with 30% stenosis at 45% of the cardiac cycle (Ciri et al. 2018). The WSS is ~22Pa and ~25Pa at the minimum lumen diameter and both below 1.2Pa downstream of the maximum stenosis in (Ciri et al. 2018) and CAFe, respectively.

At the tissue-level, our results are within the range of remodeling seen in experimental studies and clinical observations of atherosclerosis progression. For example, Pelosi et al. studied atherogenesis in porcine coronary arteries with a high cholesterol diet over the course of 4 months and observed an average increase of 1.93 mm^2 in cross-sectional area (Pelosi et al. 2014). Our model estimates a 1.87 mm^2 increase in mean cross-sectional plaque area over a course of 4 months. Additionally, our model estimates plaque growth rates comparable to a human clinical trial investigating plaque growth while on Atorvastatin (Timmins et al. 2017). Specifically, plaque area under regions of low (<1Pa) WSS increased by 0.007 mm^2 over 6 months of the trial or 0.0035 mm^2 over the last 4.5 months our simulation. Moreover, high (>2.5Pa) WSS caused plaque regression in both the trail and our model. Thus, our simulated results roughly corroborate with an experimental porcine model and clinical values of plaque growth at the tissue-level.

However, the CAFe framework has limitations. The idealized geometric and Neo-Hookean material simplifications within the mechanical models, while necessary for computational feasibility, does not capture all the nuances of the complex human arterial behavior. Although the arterial deformations seen herein were relatively small, when available for atherosclerotic tissue, utilizing material models that incorporate fibers, anisotropy, or larger deformations may increase the accuracy of the model. Our model also incorporates a wide range of physiological processes which are dependent on the initial conditions and parameters. These values were derived from existing literature and may not fully capture clinical variability. For example, the initial percent composition of each tissue type had to be determined from qualitative observations (Liu et al. 2011; Villiger et al. 2018; Wagenseil and Mecham 2009) rather than experimental findings due to the rarity and variance in values reported across sources in the literature. As

another example, for the healthy artery, there was a 7.9% overall decrease in VSMCs with the majority occurring within the first 10 simulation steps which suggests the initial conditions were not at homeostasis. After which the number of VSMCs amount stabilizes which is in line with the adaptation phenomenon that keeps a physiological VSMC/fibroblast ratio, in agreement with the hypothesis that the relative arterial cell/ECM composition does not undergo extreme changes over time (Corti et al. 2023). Additionally, 6 months is not long enough to observe an increase in stenosis. Indeed, coronary plaques often take years to produce noticeable changes in size. For example, a longitudinal 2-year study with 95 patients found the total plaque volume in patients with normal systolic blood pressure increased in volume by just 0-2.2mm^3 per year (Won et al. 2022). Yet the 6-month duration was chosen to observe intra-plaque remodeling while enabling rapid model development (as a 6-month simulation took roughly 15 and 27 hrs for non-stenotic and stenotic cases, respectively).

5. Conclusion

In conclusion, the CAFe model represents a significant step forward in the simulation of CAD progression and offers a promising tool for advancing our understanding of the disease. This multi-physics, multi-scale approach allows for a more comprehensive prediction of disease pathways, potentially leading to targeted interventions that could preempt disease progression in individual patients. Notably, the CAFe model could replicate real-world conditions within a controlled simulation environment, allowing us to observe how key factors such WSS and mechanical stress influence plaque development and remodeling. By continuing to refine this model, we hope to better predict the progression of atherosclerosis, tailor interventions to individual patients, and ultimately improve outcomes in the treatment of the disease.

Acknowledgments and Funding

The authors would like to thank Dr. Stefano Leonardi of the Mechanical Engineering Department at UT Dallas for his expertise and help with the development and implementation of the CFD module. The authors also gratefully acknowledge funding for this work provided by the National Heart, Lung, And Blood Institute of the National Institutes of Health (1R01HL136776-01A1). The content is solely the responsibility of the authors and does not necessarily represent the official views of the National Institutes of Health. AC is funded by the National Plan for NRRP Complementary Investments (PNC, established with the decree-law 6 May 2021, n. 59, converted by law n. 101 of 2021) in the call for the funding of research initiatives for technologies and innovative trajectories in the health and care sectors (Directorial Decree n. 931 of 06-06-2022) - project n. PNC0000003 - AdvaNced Technologies for Human-centrEd Medicine (ANTHEM). This work reflects only the authors' views and opinions, neither the Ministry for University and Research nor the European Commission can be considered responsible for them.

Supplemental Materials

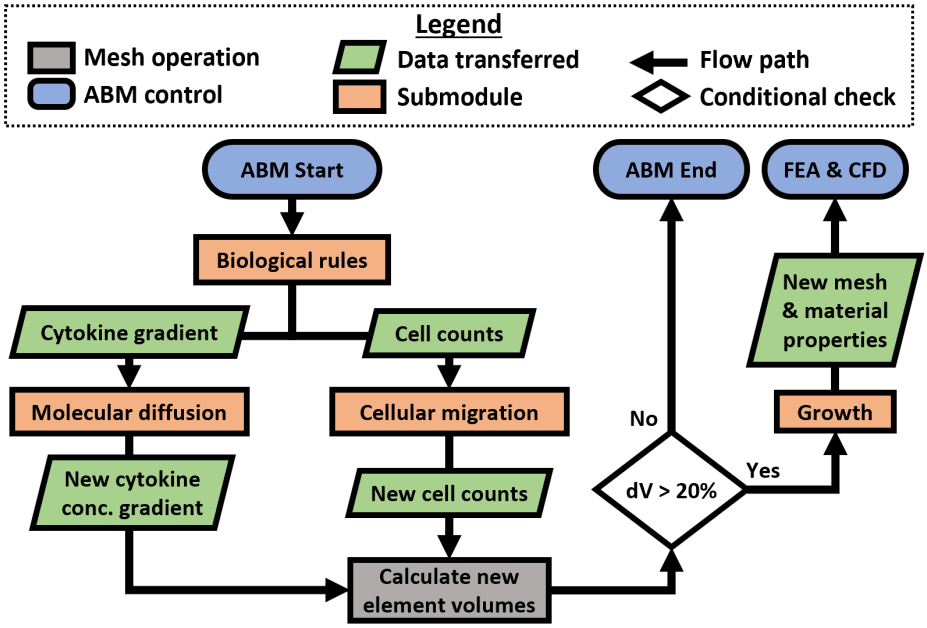

Supplemental Figure 1. Flowchart of the ABM module. Literature-derived equations govern the biological interactions and processes which modify the cytokine gradient and number of cells in each patch. A PDE solver computes the second order diffusion equation for each molecular agent and an in-house algorithm is used to simulate cellular migration. Updated values are used to calculate the new volume of each patch and determine if the mesh needs to be modified via the growth submodule.

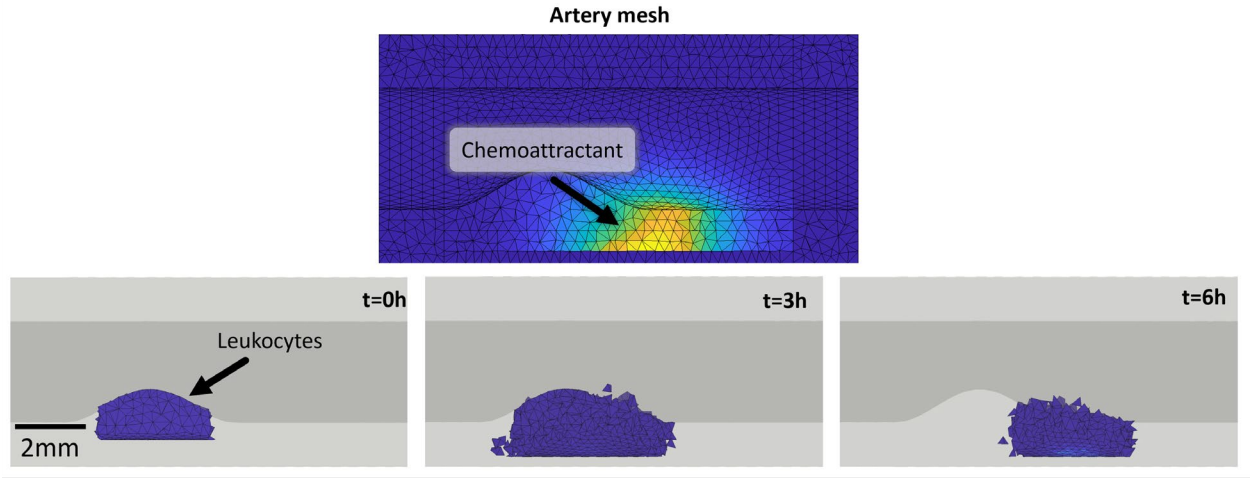

Supplemental Figure 2. Migration implementation. Individual neutrophils in patches near the source of the chemoattractant migrate up the concentration gradient over the course of 6 hours, resulting in a collective migratory pattern.

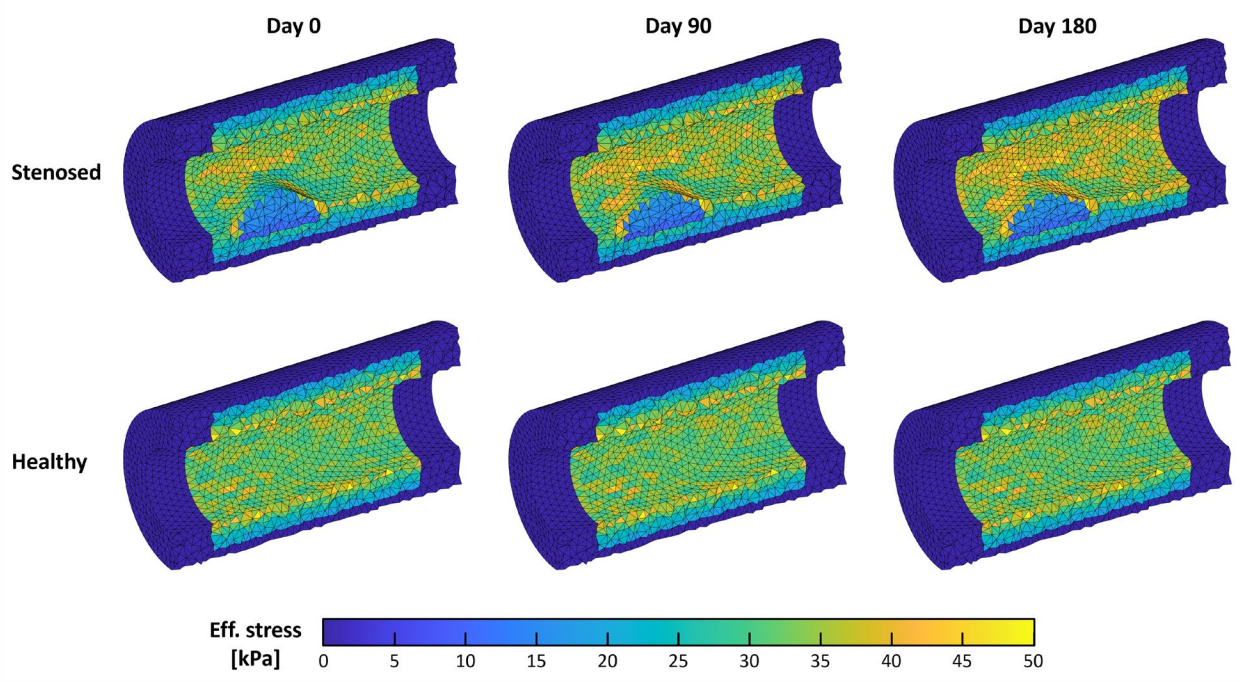

390

391 *Supplemental Figure 3. Mechanical effective stress in the healthy and stenosed cases at the beginning, middle, and end of the 6-*

392 *month period.*

393

Rule	Behavior	Equation	Ref
1	Probability of VSMC proliferation as a function of PDGFab	$P(VSMC_{prolif}) = m \cdot \left(1 - \exp\left(-\frac{P_{PDGFab}}{b}\right)\right)$ m = -3.923e-2 [h^{-1}] $b = 3818\ \left[\frac{pg}{mL}\right]$	(Li et al. 2011)
2	Probability of VSMC apoptosis	$P(VSMC_{apop})$ = 3.85e-2 [h^{-1}]	MBC
3	VSMC production of PDGFab as a function of stress	$M_{PDGFab}^{VSMC}\left[\frac{pg}{Cell \cdot h}\right] = m \cdot \sigma + b$ $m = 7.98e\text{-}8\ \left[\frac{pg}{Cell \cdot h \cdot kPa}\right]$ $b = 6.95e\text{-}6\ \left[\frac{pg}{Cell \cdot h}\right]$	(Hsieh and Frangos n.d.; Li, Moore, and Alavi 1995)
4	VSMC production of TGFβ as a function of stress	$P_{TGF\beta}^{VSMC}\left[\frac{pg}{Cell \cdot h}\right] = m \cdot \sigma + b$ $m = 2.76e\text{-}7\ \left[\frac{pg}{Cell \cdot h \cdot kPa}\right]$ b = -1.72e-5 $\left[\frac{pg}{Cell \cdot h}\right]$	(Mata-Greenwood et al. 2005; Morishita et al. 1998)
5	VSMC baseline production of MMP1	$P_{MMP1}^{VSMC}\left[\frac{pg}{Cell \cdot h}\right] = a \cdot b$ $a = 39.32\%$ (percent active) $b = 4.50e\text{-}5\ \left[\frac{pg}{Cell \cdot h}\right]$	(Karakiulakis et al. 2007; Owens, Rabinovitch, and Schwartz 1981)

6	VSMC production of MMP2 as a function of stress	$P_{MMP2}^{VSMC}\left[\frac{\text{pg}}{\text{Cell}\cdot\text{h}}\right] = a \cdot m \cdot \left(\delta + \alpha \cdot \left(1 - \exp\left(-\left(\frac{\sigma}{k}\right)^{n}\right)\right)\right)$ $a = 0.3\%$ (percent active), $m = 0.1667\left[\frac{\text{pg}}{\text{Cell}\cdot\text{h}}\right]$ (maximum rate), $\delta = 0.03, \alpha = 0.52, k = 101.55$ [kPa], $n = 2.84$	(Kim et al. 2009; Okuno et al. 2002)
7	VSMC production of MMP9 as a function of stress	$P_{MMP9}^{VSMC}\left[\frac{\text{pg}}{\text{Cell}\cdot\text{h}}\right] = a \cdot m \cdot \left(\delta + \alpha \cdot \left(1 - \exp\left(-\left(\frac{\sigma}{k}\right)^{n}\right)\right)\right)$ $a = 0.3\%$ (percent active) $m =$ 3e-4 $\left[\frac{\text{pg}}{\text{Cell}\cdot\text{h}}\right]$ (maximum rate), $\delta = 0.04,\ \alpha =$0.44, $k =$78.87 [kPa], $n =$2.88	(Garcia-Lopez et al. 2007; Kim et al. 2009)
8	VSMC production of collagen as a function of TGFβ and PDGFab	$P_{collagen}^{VSMC}\left[\frac{\text{pg}}{\text{Cell}\cdot\text{h}}\right] = \begin{cases} m \cdot P_{TGF\beta} + b, & P_{TGF\beta} > 0 \ \& \ P_{PDGFab} > 0 \\ b, & otherwise \end{cases}$ $m = 19.16$ [Cell^{-1}h^{-1}] $b = 14.98\text{e}{-4}\left[\frac{\text{pg}}{\text{Cell}\cdot\text{h}}\right]$	(Absood et al. 2004; Kim et al. 1988; Schlumberger et al. n.d.)
9	EC production of PDGFab as a function of WSS	$P_{PDGFab}^{EC}\left[\frac{\text{pg}}{\text{Cell}\cdot\text{h}}\right] = m \cdot \left(\delta + \alpha \cdot \left(1 - \exp\left(-\left(\frac{WSS}{k}\right)^{n}\right)\right)\right)$ $m = 0.104\left[\frac{\text{pg}}{\text{Cell}\cdot\text{h}}\right]$ (maximum rate) $\delta = 0.15,\ \alpha = 0.84,\ k = 2.01$ [Pa], $n = 1.24$	(Aromatario et al. 1997; Hsieh, Li, and Frangos 1991)
10	Probability of FIBRO proliferation as a function of PDGFab	$P\left(FIBRO_{prolif}\right) = a + m \cdot \left(1 - \exp\left(-\left(\frac{P_{PDGFab}}{k}\right)^{n}\right)\right)$ $a =$ 1.11e-3 [h^{-1}], $m =$ 9.41e-3 [h^{-1}], $k = 0.26$ [pg], $n =$1.29	(Wu et al. 2014; D. K. Kim et al. 1999)
11	Probability of FIBRO apoptosis	$P\left(FIBRO_{apop}\right) = 0.0105$ [h^{-1}]	MBC

12	FIBRO production of collagen as a function of strain	$P_{collagen}^{FIBRO}\left[\frac{\text{pg}}{\text{Cell}\cdot\text{h}}\right] = a\cdot\left(1+\left(m\cdot\epsilon^2+b\cdot\epsilon\right)\right)$ $a = 9.23\text{e-}3\left[\frac{\text{pg}}{\text{Cell}\cdot\text{h}}\right]$ $m = 116,\ b = 0.8$	(Wu et al. 2014; Jenkins et al. 2007)
13	FIBRO baseline production of MMP1	$P_{MMP1}^{FIBRO}\left[\frac{\text{pg}}{\text{Cell}\cdot\text{h}}\right] = 12.68e\text{-}5$	(Karakiulakis et al. 2007; Ethier, H1ckler, and Saunders 1982)
14	FIBRO baseline production of MMP2	$P_{MMP2}^{FIBRO}\left[\frac{\text{pg}}{\text{Cell}\cdot\text{h}}\right] = 7.65e\text{-}6$	(Okuno et al. 2002), MBC
15	FIBRO baseline production of MMP9	$P_{MMP9}^{FIBRO}\left[\frac{\text{pg}}{\text{Cell}\cdot\text{h}}\right] = 3.1e\text{-}7$	(Garcia-Lopez et al. 2007; Ethier, H1ckler, and Saunders 1982), MBC
16	Total PDGF-AB produced	$P_{PDGFab} = P_{PDGFab}^{VSMC} + P_{PDGFab}^{EC}$	-
17	Total TGFβ produced	$P_{TGF\beta} = P_{TGF\beta}^{VSMC}$	-
18	Total MMP1 produced	$P_{MMP1} = P_{MMP1}^{VSMC} + P_{MMP1}^{FIBRO}$	-
19	Total MMP2 produced	$P_{MMP2} = P_{MMP2}^{VSMC} + P_{MMP2}^{FIBRO}$	-
20	Total MMP9 produced	$P_{MMP9} = P_{MMP9}^{VSMC} + P_{MMP9}^{FIBRO}$	-
21	Total collagen produced	$P_{collagen} = P_{collagen}^{VSMC} + P_{collagen}^{FIBRO}$	-

22	Collagen degraded to gelatin as a function of MMP1	$25 \cdot P_{MMP1}\left[\frac{\text{pg}}{\text{h}}\right]$	(Howard G Welgus, Jeffrey, and Eisen 1981; H. G. Welgus et al. 1980)
23	Gelatin degradation as a function of MMP2	$410 \cdot P_{MMP2}\left[\frac{\text{pg}}{\text{h}}\right]$	(Xia et al. 1996; Lê et al. 1999)
24	Gelatin degradation as a function of MMP9	$135 \cdot P_{MMP9}\left[\frac{\text{pg}}{\text{h}}\right]$	(Xia et al. 1996; Murphy et al. 1985)
25	Elastin degradation as a function of MMP2	$2.64 \cdot P_{MMP2}\left[\frac{\text{pg}}{\text{h}}\right]$	(Murphy et al. 1985; Xia et al. 1996; Lê et al. 1999)
26	Elastin degradation as a function of MMP9	$0.87 \cdot P_{MMP9}\left[\frac{\text{pg}}{\text{h}}\right]$	(Murphy et al. 1985; Xia et al. 1996; Lê et al. 1999)
27	MMP1 degradation	$\frac{P_{MMP1}}{2.8}\left[\frac{\text{pg}}{\text{h}}\right]$	MBC
28	MMP2 degradation	$\frac{P_{MMP2}}{2.15}\left[\frac{pg}{h}\right]$	MBC
29	MMP9 degradation	$\frac{P_{MMP9}}{2.11}\left[\frac{pg}{h}\right]$	MBC
30	MONO adhesion as a function of TNFα x: $P_{TNF\alpha}\left[\frac{\text{U}}{\text{mL}}\right]$	$A_{MONO}^{TNF\alpha}[\text{Cells}] = \begin{cases} \frac{1}{180} \cdot \left(0.8 - 0.68 \cdot \left(1 - \exp(-0.33 \cdot \log(x)^{-0.56})\right)\right), & x > 1 \\ \frac{1}{180} \cdot 0.0996 \cdot x, & x \leq 1 \end{cases}$	(Bahra et al. 1998)

31	MONO adhesion as a function of IL1	$A_{MONO}^{IL1}[\text{Cells}] = \frac{1}{600} \cdot \left(0.14 + 0.8 \cdot \left(1 - \exp(-0.58 \cdot x^{1.19})\right)\right)$ x: $P_{IL1}\left[\frac{\text{U}}{\text{mL}}\right]$	(Bevilacqua et al. 1985)
32	MONO adhesion as a function of WSS	$A_{MONO}^{WSS}[\text{Cells}] = \frac{1}{600} \cdot (-0.3295 \cdot x^3 + 1.4 \cdot x^2 - 1.8 \cdot x + 0.79)$ x: WSS [Pa]	(Gonzales and Wick 1996)
33	Total number of MONO adhered to endothelium as a function of WSS, IL1, and TNFα	$A_{MONO}[\text{Cells}] = \begin{cases} \frac{1}{7.5} \cdot \left(A_{MONO}^{TNF\alpha} + A_{MONO}^{IL1} + A_{MONO}^{WSS}\right) \cdot t \cdot \rho \cdot V, & x < 1 \\ 0, & x \geq 1 \end{cases}$ x: WSS[Pa], ρ: Blood monocyte density $\left[\frac{\text{Cells}}{\text{mm}^3}\right]$, V: Volume [mm^3], t: 3600 [s]	-
34	Number of adhered MONO that undergo TEM as a function of stiffness	$N_{MONO} = \begin{cases} A_{MONO} \cdot (7.8\text{e-}3 \cdot x^2 + 0.048 \cdot x + 0.5106), & x < 0 \\ A_{MONO} \cdot 0.95, & x \geq 0 \end{cases}$ x: stiffness [kPa]	(Hayenga and Aranda-Espinoza 2013)
35	MONO baseline production of TNFα	$P_{TNF\alpha}^{MONO}\left[\frac{\text{U}}{\text{mL}\cdot\text{h}\cdot\text{Cell}}\right] = 6.7\text{e-}4$	(Hatanaka et al. 2006)
36	MONO baseline production of IL1	$P_{IL1}^{MONO}\left[\frac{\text{U}}{\text{mL}\cdot\text{h}\cdot\text{Cell}}\right] = 5.0\text{e-}5$	(Hatanaka et al. 2006)
37	LYMPHO adhesion as a function of TNFα	$A_{LYMPHO}^{TNF\alpha}[\text{Cells}] = \begin{cases} \frac{1}{180} \cdot \left(0.8 - 0.68 \cdot \left(1 - \exp(-0.33 \cdot \log(x)^{-0.56})\right)\right), & x > 1 \\ \frac{1}{180} \cdot 0.0996 \cdot x, & x \leq 1 \end{cases}$ x: $P_{TNF\alpha}\left[\frac{\text{U}}{\text{mL}}\right]$	(Bahra et al. 1998)
38	LYMPHO adhesion as a function of IL1	$A_{LYMPHO}^{IL1}[\text{Cells}] = \frac{1}{900} \cdot \left(0.1 + 0.19 \cdot (1 - \exp(-28.29 \cdot x^{1.46}))\right)$ x: $P_{IL1}\left[\frac{\text{U}}{\text{mL}}\right]$	(Breviario et al. 1988)
39	LYMPHO adhesion as a function of WSS	$A_{LYMPHO}^{WSS}[\text{Cells}] = \frac{1}{25} \cdot (-9.93 \cdot x^3 + 11.0 \cdot x^2 - 4.1 \cdot x + 0.55)$ x: WSS[Pa]	(Munn, Melder, and Jain 1994;

			Melder et al. 1995)
40	Total number of LYMPHO adhered to endothelium as a function of WSS, IL1, and TNFα	$A_{LYMPHO}[\text{Cells}] = \begin{cases} \frac{1}{7.5} \cdot \left(A_{LYMPHO}^{TNF\alpha} + A_{LYMPHO}^{IL1} + A_{LYMPHO}^{WSS}\right) \cdot t \cdot \rho \cdot V, & x < 0.41 \\ 0, & x \geq 0.41 \end{cases}$ $x: WSS[\text{Pa}]$, ρ: Blood lymphocyte density $\left[\frac{\text{Cells}}{\text{mm}^3}\right]$, V: Volume [mm^3], t: 3600 [s]	-
41	Number of adhered LYMPHO that undergo TEM as a function of stiffness	$N_{LYMPHO} = \begin{cases} A_{LYMPHO} \cdot (7.8\text{e-}3 \cdot x^2 + 0.048 \cdot x + 0.5106), & x < 0 \\ A_{LYMPHO} \cdot 0.95, & x \geq 0 \end{cases}$ x: stiffness[kPa]	(Hayenga and Aranda-Espinoza 2013)
42	LYMPHO baseline production of IL10	$P_{IL10}^{LYMPHO}\left[\frac{\text{U}}{\text{mL·h·Cell}}\right] = 3.75\text{e-}5$	(Rafiq et al. 2001)
43	NEUTRO adhesion as a function of TNFα	$A_{NEUTRO}^{TNF\alpha}[\text{Cells}] = \begin{cases} \frac{1}{180} \cdot \left(0.8 - 0.68 \cdot \left(1 - \exp(-0.33 \cdot \log(x)^{-0.56})\right)\right), & x > 1 \\ \frac{1}{180} \cdot 0.0996 \cdot x, & x \leq 1 \end{cases}$ $x: P_{TNF\alpha}\left[\frac{U}{mL}\right]$	(Bahra et al. 1998)
44	NEUTRO adhesion as a function of IL1	$A_{NEUTRO}^{IL1}[\text{Cells}] = \frac{1}{900} \cdot \left(0.1 + 0.19 \cdot (1 - \exp(-28.29 \cdot x^{1.46}))\right)$ $x: P_{IL1}\left[\frac{\text{U}}{\text{mL}}\right]$	(Breviario et al. 1988)
45	NEUTRO adhesion as a function of WSS	$A_{NEUTRO}^{WSS}[\text{Cells}] = \frac{1}{300} \cdot (0.26 \cdot x^2 - 0.8 \cdot x + 0.63)$ $x: WSS[\text{Pa}]$	(Sheikh et al. 2003)
46	Total number of NEUTRO adhered to endothelium as a function of WSS, IL1, and TNFα	$A_{NEUTRO}[\text{Cells}] = \begin{cases} \frac{1}{7.5} \cdot \left(A_{NEUTRO}^{TNF\alpha} + A_{NEUTRO}^{IL1} + A_{NEUTRO}^{WSS}\right) \cdot t \cdot \rho \cdot V, & x < 1.2 \\ 0, & x \geq 1.2 \end{cases}$ $x: WSS[\text{Pa}]$, ρ: Blood neutrophil density $\left[\frac{\text{Cells}}{\text{mm}^3}\right]$, V: Volume [mm^3], t: 3600 [s]	-

47	Number of adhered NEUTRO that undergo TEM as a function of stiffness	$N_{NEUTRO} = \begin{cases} A_{NEUTRO} \cdot (9.18\text{e-}2 \cdot x + 0.456), & x < 5 \\ A_{NEUTRO} \cdot 0.91, & x \geq 5 \end{cases}$ x: stiffness[kPa]	(Stroka and Aranda-Espinoza 2011)
48	NEUTRO baseline production of TNFα	$P_{TNF\alpha}^{NEUTRO}\left[\frac{\text{U}}{\text{mL}\cdot\text{h}\cdot\text{Cell}}\right] = 5.0\text{e-}6$	(Hatanaka et al. 2006)
49	NEUTRO baseline production of IL1	$P_{IL1}^{NEUTRO}\left[\frac{\text{U}}{\text{mL}\cdot\text{h}\cdot\text{Cell}}\right] = 5.0\text{e-}7$	(Hatanaka et al. 2006)
50	Total TNF-α produced	$P_{TNF\alpha}\left[\frac{\text{U}}{\text{mL}\cdot\text{h}\cdot\text{Cell}}\right] = P_{TNF\alpha}^{MONO} + P_{TNF\alpha}^{NEUTRO}$	-
51	Total IL1 produced	$P_{IL1}\left[\frac{\text{U}}{\text{mL}\cdot\text{h}\cdot\text{Cell}}\right] = P_{IL1}^{MONO} + P_{IL1}^{NEUTRO}$	-
52	Total IL10 produced	$P_{IL10}\left[\frac{\text{U}}{\text{mL}\cdot\text{h}\cdot\text{Cell}}\right] = P_{IL10}^{LYMPHO}$	-
53	Concentration of LDL at endothelium as a function of WSS	$C_{LDL}\left[\frac{\text{pg}}{\text{mm}^3}\right]$ $= \begin{cases} C_0 \cdot (2\text{e-}8\cdot x^6 - 2\text{e-}6\cdot x^5 + 6\text{e-}5\cdot x^4 - 1.1\text{e-}3\cdot x^3 + 1.04\text{e-}2x^2 - 0.05x + 0.096), & x < 5 \\ 0, & x \geq 5 \end{cases}$ x: WSS [Pa], C_0: Blood LDL concentration $\left[\frac{\text{pg}}{\text{mm}^3}\right]$	(Deng et al. 1995)
54	LDL infiltration into wall	$P_{LDL}\left[\frac{\text{pg}}{\text{mm}^3}\right] = 0.7 \cdot C_{LDL}$ 70% of LDL at the lumen	(Deng et al. 1995)
55	LDL oxidation rate	$C_{oxLDL}\left[\frac{\text{pg}}{\text{mm}^3}\right] = 0.012 \cdot P_{LDL}$ 1.2% per hour	(Pappalardo, Musumeci, and Motta 2008)
56	MONO to MACRO ratio	$N_{MACRO} = \frac{1}{2} \cdot N_{MONO}$ Upon entering the wall, monocytes differentiate into macrophages	(Adamson and Leitinger 2011; Colin, Chinetti-Gbaguidi, and

			Staels 2014; Ley, Miller, and Hedrick 2011; Kadl et al. 2010)
57	MACRO LDL consumption	$16.67\left[\frac{\text{pg}}{\text{h}}\right]$	(Leake and Rankin 1990)
58	MACRO to FOAM transition	If a macrophage consumes >500 pg LDL, it turns into a foam cell	(Dubland and Francis 2015)
59	Effective (von-Mises) stress	$\sigma = \sqrt{0.5 \cdot \left(\left(s_x - s_y\right)^2 + \left(s_y - s_z\right)^2 + (s_x - s_z)^2 + 6 \cdot \left({s_{xy}}^2 + {s_{yz}}^2 + {s_{xz}}^2\right)\right)}$ s_x: xx-component of Cauchy stress s_y: yy-component of Cauchy stress s_z: zz-component of Cauchy stress s_{xy}: xy-component of Cauchy stress s_{yz}: yz-component of Cauchy stress s_{xz}: xz-component of Cauchy stress	-
60	Effective (Green-Lagrange) strain	$\epsilon = \sqrt{{E_x}^2 + {E_y}^2 + {E_z}^2 - E_{xy} \cdot E_{xz} - E_{xy} \cdot E_{yz} - E_{yz} \cdot E_{xz} + 3 \cdot \left({E_{xy}}^2 + {E_{xz}}^2 + {E_{yz}}^2\right)}$ E_x: xx-component of Green-Lagrange strain E_y: yy-component of Green-Lagrange strain E_z: zz-component of Green-Lagrange strain E_{xy}: xy-component of Green-Lagrange strain E_{yz}: yz-component of Green-Lagrange strain E_{xz}: xz-component of Green-Lagrange strain	-

394 *Supplemental Table 1. ABM Rules.*

395

References

Ateshian, Gerard A, Barclay Morrison, Jeffrey W Holmes, and Clark T Hung. 2012. 'Mechanics of Cell Growth.' *Mechanics Research Communications* 42 (June):118–25. https://doi.org/10.1016/j.mechrescom.2012.01.010.

Bhui, Rita, and Heather N. Hayenga. 2017. 'An Agent-Based Model of Leukocyte Transendothelial Migration during Atherogenesis'. *PLoS Computational Biology* 13 (5). https://doi.org/10.1371/journal.pcbi.1005523.

Blewett, Lynn A., Julia A. Rivera Drew, Risa Griffin, Natalie Del Ponte, and Pat Convey. 2021. 'Medical Expenditure Panel Survey, Version 2.1'. *Https://Meps.Ipums.Org*. Minneapolis, MN: IPUMS.

Blumenreich, Martin S. 1990. *The White Blood Cell and Differential Count*.

Bufi, Nathalie, Michael Saitakis, Stéphanie Dogniaux, Oscar Buschinger, Armelle Bohineust, Alain Richert, Mathieu Maurin, Claire Hivroz, and Atef Asnacios. 2015. 'Human Primary Immune Cells Exhibit Distinct Mechanical Properties That Are Modified by Inflammation'. *Biophysical Journal* 108 (9): 2181–90. https://doi.org/10.1016/j.bpj.2015.03.047.

Cano, Patricia M., Amandine Vargas, and Jean-Pierre Lavoie. 2016. 'A Real-Time Assay for Neutrophil Chemotaxis'. *BioTechniques* 60 (5): 245–51. https://doi.org/10.2144/000114416.

Ciri, Umberto, Rita Bhui, Jorge Bailon-Cuba, Heather N. Hayenga, and Stefano Leonardi. 2018. 'Dependence of Leukocyte Capture on Instantaneous Pulsatile Flow'. *Journal of Biomechanics* 76 (July):84–93. https://doi.org/10.1016/j.jbiomech.2018.05.044.

Corti, Anna, Stefano Casarin, Claudio Chiastra, Monika Colombo, Francesco Migliavacca, and Marc Garbey. 2019. 'A Multiscale Model of Atherosclerotic Plaque Development: Toward a Coupling Between an Agent-Based Model and CFD Simulations'. In , 410–23. https://doi.org/10.1007/978-3-030-22747-0_31.

Corti, Anna, Claudio Chiastra, Monika Colombo, Marc Garbey, Francesco Migliavacca, and Stefano Casarin. 2020. 'A Fully Coupled Computational Fluid Dynamics – Agent-Based Model of Atherosclerotic Plaque Development: Multiscale Modeling Framework and Parameter Sensitivity Analysis'. *Computers in Biology and Medicine* 118 (March):103623. https://doi.org/10.1016/j.compbiomed.2020.103623.

Corti, Anna, Monika Colombo, Francesco Migliavacca, Scott A. Berceli, Stefano Casarin, Jose F. Rodriguez Matas, and Claudio Chiastra. 2022. 'Multiscale Agent-Based Modeling of Restenosis after Percutaneous Transluminal Angioplasty: Effects of Tissue Damage and Hemodynamics on Cellular Activity'. *Computers in Biology and Medicine* 147 (August):105753. https://doi.org/10.1016/j.compbiomed.2022.105753.

Corti, Anna, Monika Colombo, Francesco Migliavacca, Jose Felix Rodriguez Matas, Stefano Casarin, and Claudio Chiastra. 2021. 'Multiscale Computational Modeling of Vascular Adaptation: A Systems Biology Approach Using Agent-Based Models'. *Frontiers in Bioengineering and Biotechnology* 9 (November). https://doi.org/10.3389/fbioe.2021.744560.

Corti, Anna, Matilde Marradi, Cemre Çelikbudak Orhon, Francesca Boccafoschi, Philippe Büchler, Jose F. Rodriguez Matas, and Claudio Chiastra. 2024. 'Impact of Tissue Damage and Hemodynamics on Restenosis Following Percutaneous Transluminal Angioplasty: A Patient-Specific Multiscale Model'. *Annals of Biomedical Engineering* 52 (8): 2203–20. https://doi.org/10.1007/s10439-024-03520-1.

Corti, Anna, Francesco Migliavacca, Scott A. Berceli, and Claudio Chiastra. 2023. 'Predicting 1-Year in-Stent Restenosis in Superficial Femoral Arteries through Multiscale Computational Modelling'. *Journal of The Royal Society Interface* 20 (201). https://doi.org/10.1098/rsif.2022.0876.

Cury, Ricardo C., Suhny Abbara, Stephan Achenbach, Arthur Agatston, Daniel S. Berman, Matthew J. Budoff, Karin E. Dill, et al. 2016. 'CAD-RADSTM Coronary Artery Disease – Reporting and Data System. An Expert Consensus Document of the Society of Cardiovascular Computed Tomography (SCCT), the American College of Radiology (ACR) and the North American Society for Cardiovascular Imaging (NASCI). Endorsed by the American College of Cardiology'. *Journal of Cardiovascular Computed Tomography* 10 (4): 269–81. https://doi.org/10.1016/j.jcct.2016.04.005.

Deng, Xiaoyan, Yves Marois, Yahye Merhi, Martin King, R O B E R T Guidoin, and Robert Guidoin. 1995. 'Luminal Surface Concentration of Lipoprotein (LDL) and Its Effect on the Wall Uptake of Cholesterol by Canine Carotid Arteries'.

Engler, Adam J., Maureen A. Griffin, Shamik Sen, Carsten G. Bönnemann, H. Lee Sweeney, and Dennis E. Discher. 2004. 'Myotubes Differentiate Optimally on Substrates with Tissue-like Stiffness'. *Journal of Cell Biology* 166 (6): 877–87. https://doi.org/10.1083/jcb.200405004.

Eshtehardi, Parham, Michael C McDaniel, Saurabh S Dhawan, José Nilo G Binongo, Sandeep K Krishnan, Lucas Golub, Michel T Corban, Paolo Raggi, Arshed A Quyyumi, and Habib Samady. 2012. 'Effect of Intensive Atorvastatin Therapy on Coronary Atherosclerosis Progression, Composition, Arterial Remodeling, and Microvascular Function.' *The Journal of Invasive Cardiology* 24 (10): 522–29.

Expert Panel on Detection, Evaluation, and Treatment of High Blood Cholesterol in Adults. 2001. 'Executive Summary of the Third Report of the National Cholesterol Education Program (NCEP) Expert Panel on Detection, Evaluation, and Treatment of High Blood Cholesterol in Adults (Adult Treatment Panel III)'. *JAMA: The Journal of the American Medical Association* 285 (19): 2486–97. https://doi.org/10.1001/jama.285.19.2486.

Farrell, Brian E., Ronald P. Daniele, and Douglas A. Lauffenburger. 1990. 'Quantitative Relationships between Single-cell and Cell-population Model Parameters for Chemosensory Migration Responses of Alveolar Macrophages to C5a'. *Cell Motility* 16 (4): 279–93. https://doi.org/10.1002/cm.970160407.

Gay, Cyril G., and Jeffrey A. Winkles. 1991. 'The Half-Lives of Platelet-Derived Growth Factor A- and B-Chain MRNAS Are Similar in Endothelial Cells and Unaffected by Heparin-Binding Growth Factor-1 or Cycloheximide'. *Journal of Cellular Physiology* 147 (1): 121–27. https://doi.org/10.1002/jcp.1041470116.

Gradus-Pizlo, Irmina, and Harvey Feigenbaum. 2003. 'Potential Use of High-Resolution Two-Dimensional Transthoracic Echocardiography for Visualization of the Left Anterior Descending Coronary Artery'. *The American Heart Hospital Journal* 1 (1): 77–82. https://doi.org/10.1111/j.1541-9215.2003.02101.x.

Guvenir Torun, Su, Hakki M. Torun, Hendrik H. G. Hansen, Giulia Gandini, Irene Berselli, Veronica Codazzi, Chris L. de Korte, et al. 2021. 'Multicomponent Mechanical Characterization of Atherosclerotic Human Coronary Arteries: An Experimental and Computational Hybrid Approach'. *Frontiers in Physiology* 12 (September). https://doi.org/10.3389/fphys.2021.733009.

Hazuda, D J, J C Lee, and P R Young. 1988. 'The Kinetics of Interleukin 1 Secretion from Activated Monocytes. Differences between Interleukin 1 Alpha and Interleukin 1 Beta.' *Journal of Biological Chemistry* 263 (17): 8473–79. https://doi.org/10.1016/S0021-9258(18)68502-3.

He, Xiaoyi, and David N. Ku. 1996. 'Pulsatile Flow in the Human Left Coronary Artery Bifurcation: Average Conditions'. *Journal of Biomechanical Engineering* 118 (1): 74–82. https://doi.org/10.1115/1.2795948.

Karšaj, I., J. Sorić, and J.D. Humphrey. 2010. 'A 3-D Framework for Arterial Growth and Remodeling in Response to Altered Hemodynamics'. *International Journal of Engineering Science* 48 (11): 1357–72. https://doi.org/10.1016/j.ijengsci.2010.06.033.

Keshavarzian, Maziyar, Clark A. Meyer, and Heather N. Hayenga. 2018. 'Mechanobiological Model of Arterial Growth and Remodeling'. *Biomechanics and Modeling in Mechanobiology* 17 (1): 87–101. https://doi.org/10.1007/s10237-017-0946-y.

Konishi, Takao, Saikat Kumar B. Ghosh, Yu Sato, Rika Kawakami, Kenji Kawai, Aimee E. Vozenilek, Weili Xu, et al. 2023. 'The Histological Analysis of the Coronary Medial Thickness: Implications for Percutaneous Coronary Intervention'. *PLOS ONE* 18 (3): e0283840. https://doi.org/10.1371/journal.pone.0283840.

Lee, Yong J., Dipika Patel, and Soyeun Park. 2011. 'Local Rheology of Human Neutrophils Investigated Using Atomic Force Microscopy'. *International Journal of Biological Sciences* 7 (1): 102–11. https://doi.org/10.7150/ijbs.7.102.

Liu, Linbo, Joseph A. Gardecki, Seemantini K. Nadkarni, Jimmy D. Toussaint, Yukako Yagi, Brett E. Bouma, and Guillermo J. Tearney. 2011. 'Imaging the Subcellular Structure of Human Coronary Atherosclerosis Using Micro-Optical Coherence Tomography'. *Nature Medicine* 17 (8): 1010–14. https://doi.org/10.1038/nm.2409.

Lou, Xia, and Traian V. Chirila. 1999. 'Swelling Behavior and Mechanical Properties of Chemically Cross-Linked Gelatin Gels for Biomedical Use'. *Journal of Biomaterials Applications* 14 (2): 184–91. https://doi.org/10.1177/088532829901400204.

Lu, Hannah, Kimoon Um, and Daniel M. Tartakovsky. 2021. 'Hybrid Models of Chemotaxis with Application to Leukocyte Migration'. *Journal of Mathematical Biology* 82 (4). https://doi.org/10.1007/s00285-021-01581-7.

Lu, Qijin, Kavitha Ganesan, Dan T. Simionescu, and Narendra R. Vyavahare. 2004. 'Novel Porous Aortic Elastin and Collagen Scaffolds for Tissue Engineering'. *Biomaterials* 25 (22): 5227–37. https://doi.org/10.1016/j.biomaterials.2003.12.019.

Maas, Steve A, Benjamin J Ellis, Gerard A Ateshian, and Jeffrey A Weiss. 2012. 'FEBio: Finite Elements for Biomechanics.' *Journal of Biomechanical Engineering* 134 (1): 011005. https://doi.org/10.1115/1.4005694.

Mallol, Roger, Miguel A. Rodríguez, Mercedes Heras, Maria Vinaixa, Núria Plana, Lluís Masana, Gareth A. Morris, and Xavier Correig. 2012. 'Particle Size Measurement of Lipoprotein Fractions Using Diffusion-Ordered NMR Spectroscopy'. *Analytical and Bioanalytical Chemistry* 402 (7): 2407–15. https://doi.org/10.1007/s00216-011-5705-9.

Moghe, Prabhas V., Robert D. Nelson, and Robert T. Tranquillo. 1995. 'Cytokine-Stimulated Chemotaxis of Human Neutrophils in a 3-D Conjoined Fibrin Gel Assay'. *Journal of Immunological Methods* 180 (2): 193–211. https://doi.org/10.1016/0022-1759(94)00314-M.

Norris, T. O., and John McGraw. 1964. 'Gelatin Coatings and Tensile Strength of Gelatin Films'. *Journal of Applied Polymer Science* 8 (5): 2139–45. https://doi.org/10.1002/app.1964.070080514.

Nosovitsky, Victor A., Olusegun J. Ilegbusi, Joseph Jiang, Peter H. Stone, and Charles L. Feldman. 1997. 'Effects of Curvature and Stenosis-Like Narrowing on Wall Shear Stress in a Coronary Artery Model with Phasic Flow'. *Computers and Biomedical Research* 30 (1): 61–82. https://doi.org/10.1006/cbmr.1997.1434.

Patel, Naimish R., Medhavi Bole, Cheng Chen, Charles C. Hardin, Alvin T. Kho, Justin Mih, Linhong Deng, et al. 2012. 'Cell Elasticity Determines Macrophage Function'. *PLoS ONE* 7 (9): e41024. https://doi.org/10.1371/journal.pone.0041024.

Pelosi, Gualtiero, Silvia Rocchiccioli, Antonella Cecchettini, Federica Viglione, Mariarita Puntoni, Oberdan Parodi, Enrico Capobianco, and Maria G. Trivella. 2014. 'Inflammation Blood and Tissue Factors of Plaque Growth in an Experimental Model Evidenced by a Systems Approach'. *Frontiers in Genetics* 5 (April). https://doi.org/10.3389/fgene.2014.00070.

Qiu, Hongyu, Yi Zhu, Zhe Sun, Jerome P. Trzeciakowski, Meredith Gansner, Christophe Depre, Ranillo R.G. Resuello, et al. 2010. 'Short Communication: Vascular Smooth Muscle Cell Stiffness As a Mechanism for Increased Aortic Stiffness With Aging'. *Circulation Research* 107 (5): 615–19. https://doi.org/10.1161/CIRCRESAHA.110.221846.

Rangarajan, Rajagopal, and Muhammad H. Zaman. 2008. 'Modeling Cell Migration in 3D'. *Cell Adhesion & Migration* 2 (2): 106–9. https://doi.org/10.4161/cam.2.2.6211.

Rapp, Bastian E. 2017. 'Engineering Mathematics'. In *Microfluidics: Modelling, Mechanics and Mathematics*, 21–50. Elsevier. https://doi.org/10.1016/B978-1-4557-3141-1.50003-4.

Samady, Habib, Parham Eshtehardi, Michael C. McDaniel, Jin Suo, Saurabh S. Dhawan, Charles Maynard, Lucas H. Timmins, Arshed A. Quyyumi, and Don P. Giddens. 2011. 'Coronary Artery Wall Shear Stress Is Associated With Progression and Transformation of Atherosclerotic Plaque and Arterial Remodeling in Patients With Coronary Artery Disease'. *Circulation* 124 (7): 779–88. https://doi.org/10.1161/CIRCULATIONAHA.111.021824.

Si, Hang. 2015. 'TetGen, a Delaunay-Based Quality Tetrahedral Mesh Generator'. *ACM Transactions on Mathematical Software* 41 (2): 1–36. https://doi.org/10.1145/2629697.

Smedby, Örjan. 1997. 'Do Plaques Grow Upstream or Downstream?' *Arteriosclerosis, Thrombosis, and Vascular Biology* 17 (5): 912–18. https://doi.org/10.1161/01.ATV.17.5.912.

Stroka, Kimberly M., and Helim Aranda-Espinoza. 2011. 'Endothelial Cell Substrate Stiffness Influences Neutrophil Transmigration via Myosin Light Chain Kinase-Dependent Cell Contraction'. *Blood* 118 (6): 1632–40. https://doi.org/10.1182/blood-2010-11-321125.

Svetkey, Laura P, David W Harsha, William M Vollmer, Victor J Stevens, Eva Obarzanek, Patricia J Elmer, Pao-Hwa Lin, et al. 2003. 'Premier: A Clinical Trial of Comprehensive Lifestyle Modification for Blood Pressure Control: Rationale, Design and Baseline Characteristics'. *Annals of Epidemiology* 13 (6): 462–71. https://doi.org/10.1016/S1047-2797(03)00006-1.

Thorne, Bryan C., Heather N. Hayenga, Jay D. Humphrey, and Shayn M. Peirce. 2011. 'Toward a Multi-Scale Computational Model of Arterial Adaptation in Hypertension: Verification of a Multi-Cell Agent-Based Model'. *Frontiers in Physiology* MAY. https://doi.org/10.3389/fphys.2011.00020.

Timmins, Lucas H., David S. Molony, Parham Eshtehardi, Michael C. McDaniel, John N. Oshinski, Don P. Giddens, and Habib Samady. 2017. 'Oscillatory Wall Shear Stress Is a Dominant Flow Characteristic Affecting Lesion Progression Patterns and Plaque Vulnerability in Patients with Coronary Artery Disease'. *Journal of the Royal Society Interface* 14 (127). https://doi.org/10.1098/rsif.2016.0972.

562 Tsao, Connie W., Aaron W. Aday, Zaid I. Almarzooq, Alvaro Alonso, Andrea Z. Beaton, Marcio S. Bittencourt,
563 Amelia K. Boehme, et al. 2022. 'Heart Disease and Stroke Statistics—2022 Update: A Report From
564 the American Heart Association'. *Circulation* 145 (8).
565 https://doi.org/10.1161/CIR.0000000000001052.

566 Tziotziou, Aikaterini, Eline Hartman, Suze-Anne Korteland, Aad van der Lugt, Antonius F.W. van der Steen,
567 Joost Daemen, Daniel Bos, Jolanda Wentzel, and Ali C. Akyildiz. 2023. 'Mechanical Wall Stress and
568 Wall Shear Stress Are Associated with Atherosclerosis Development in Non-Calcified Coronary
569 Segments'. *Atherosclerosis* 387 (December):117387.
570 https://doi.org/10.1016/j.atherosclerosis.2023.117387.

571 Villiger, Martin, Kenichiro Otsuka, Antonios Karanasos, Pallavi Doradla, Jian Ren, Norman Lippok, Milen
572 Shishkov, et al. 2018. 'Coronary Plaque Microstructure and Composition Modify Optical Polarization:
573 A New Endogenous Contrast Mechanism for Optical Frequency Domain Imaging'. *JACC:*
574 *Cardiovascular Imaging* 11 (11): 1666–76. https://doi.org/10.1016/j.jcmg.2017.09.023.

575 Wagenseil, Jessica E., and Robert P. Mecham. 2009. 'Vascular Extracellular Matrix and Arterial Mechanics'.
576 *Physiological Reviews*. https://doi.org/10.1152/physrev.00041.2008.

577 Warren, Jeremy L., John E. Yoo, Clark A. Meyer, David S. Molony, Habib Samady, and Heather N. Hayenga.
578 2022. 'Automated Finite Element Approach to Generate Anatomical Patient-Specific Biomechanical
579 Models of Atherosclerotic Arteries from Virtual Histology-Intravascular Ultrasound'. *Frontiers in*
580 *Medical Technology* 4 (November). https://doi.org/10.3389/fmedt.2022.1008540.

581 Won, Ki-Bum, Hyung-Bok Park, Ran Heo, Byoung Kwon Lee, Fay Y. Lin, Martin Hadamitzky, Yong-Jin Kim, et
582 al. 2022. 'Longitudinal Quantitative Assessment of Coronary Atherosclerosis Related to Normal
583 Systolic Blood Pressure Maintenance in the Absence of Established Cardiovascular Disease'. *Clinical*
584 *Cardiology* 45 (8): 873–81. https://doi.org/10.1002/clc.23870.

585 Yakimets, Iryna, Nikolaus Wellner, Andrew C. Smith, Reginald H. Wilson, Imad Farhat, and John Mitchell.
586 2005. 'Mechanical Properties with Respect to Water Content of Gelatin Films in Glassy State'. *Polymer*
587 46 (26): 12577–85. https://doi.org/10.1016/j.polymer.2005.10.090.

588 Zaman, Muhammad H., Roger D. Kamm, Paul Matsudaira, and Douglas A. Lauffenburger. 2005.
589 'Computational Model for Cell Migration in Three-Dimensional Matrices'. *Biophysical Journal* 89 (2):
590 1389–97. https://doi.org/10.1529/biophysj.105.060723.

591